Chemical Engineering Science 64 (2009) 1784 – 1797

Contents lists available at ScienceDirect

Chemical Engineering Science

journal homepage: www.elsevier.com/locate/ces

A model for collisional exchange in gas/liquid/solid fluidized beds

Peter J. O'Rourke[a,*], Paul (Pinghua) Zhao[b], Dale Snider[b]

[a]CFD d'OR Software and Consulting, LLC, USA
[b]CPFD Software, LLC, USA

ARTICLE INFO

Article history:
Received 21 June 2008
Received in revised form 15 October 2008
Accepted 14 December 2008
Available online 25 December 2008

Keywords:
CPFD
Fluidization
Mathematical modeling
Multiphase flow
Particle collisions
Particle processing

ABSTRACT

A new model is presented for numerical simulations of collisional transfer of mass, momentum and energy in gas/liquid/solid fluidized beds. The mathematical formulation uses a collision model similar to that of Bhatnagar, Gross, and Krook (BGK), in a particle distribution function transport equation, in order to approximate the rates at which collisions bring about local equilibration of particle velocities and the masses, compositions, and temperatures of liquid films on bed particles. The model is implemented in the framework of the computational-particle fluid dynamics (CPFD) numerical methodology, in which the particle phase is represented with computational parcels and the continuous phase is calculated on Eulerian finite-difference grid. Computational examples using the Barracuda® code, a commercial CFD code owned by CPFD Software, LLC, show the ability of the model to calculate spray injection and subsequent liquid spreading in gas/solid flows.

1. Introduction

Gas/liquid/solid fluidized beds are used in fluid cokers to convert a heavy hydrocarbon feed into lighter hydrocarbon components, gases, and coke (Song et al., 2004; Gray et al., 2004). The liquid hydrocarbon feed is introduced as a spray that wets hot solid bed particles. The heated feed then reacts in the liquid phase to form lighter weight components, coke, and, possibly, some vapor; and the lighter-weight components vaporize at the surfaces of liquid films on the particles. The solid bed particles provide a large surface area upon which rapid heat transfer to the liquid hydrocarbon can occur. Gas/liquid/solid beds are also used in fluidized bed granulators to produce solids from liquid products such as solutions and suspensions (Heinrich et al., 2003).

In such a fluidized bed, collisions between liquid spray droplets and bed particles, and between the wet bed particles themselves, are the mechanisms whereby the liquid spreads over the particles' surfaces. More generally, collisions result in mass, momentum, and energy transfer between particles and cause a variety of associated physical effects. Momentum transfer results in the damping of relative motion between particles, which, in turn, reduces the collision frequency. In addition to spreading the liquid over the particles' surfaces, collisional mass transfer results in mixing of liquid residing on different particles and to a tendency toward local uniformity of liquid chemical composition and liquid temperature on different particles.

In this paper we document a unified model for collisional mass, momentum, and energy transfer between bed particles in a gas/liquid/solid fluidized bed. The mathematical model extends the equations of the multiphase particle-in-cell (MP-PIC) method (Andrews and O'Rourke, 1996; Snider et al., 1998; Snider, 2001) by including collision terms on the right-hand side of the transport equation for the single-particle distribution function for the bed particles. The form of the collision terms is the same as in the Bhatnagar, Gross, and Krook (BGK) model for collisions in the Boltzmann equation of gas dynamics (Vincenti and Kruger, 1975). In the BGK model, the effect of collisions is represented by a simple relaxation term on the right-hand side of the Boltzmann equation that is the difference between the current value of the molecular distribution function and the equilibrium Boltzmann velocity distribution, divided by a molecular collision time. In this work, the equilibrium distributions involve delta functions of particle properties, reflecting the fact that particle collisions damp fluctuations in particle properties.

An effect related to particle collisions is already included in the MP-PIC equations, and this is the effect of an isotropic particle collisional pressure (Andrews and O'Rourke, 1996; Snider et al., 1998; Snider, 2001). Gradients in this pressure result in particle accelerations that prevent particle volume fractions from exceeding their close-pack limit. Particle collisions also result in particle stresses that depend either linearly, or quadratically, on gradients in particle velocity fields (Savage and Jeffrey, 1981; Lun et al., 1984). In contrast, the new collision effects in this study are purely local in the sense that they affect only the local distributions of particle properties, and do not involve spatial gradients of particle properties. We also note

* Corresponding author. Tel.: +1 505 663 0524.
E-mail address: cfddor@swcp.com (P.J. O'Rourke).

0009-2509/$ - see front matter © 2009 Elsevier Ltd. All rights reserved.
doi:10.1016/j.ces.2008.12.014

that in previous work the effects of particle collisions have been represented in numerical models for dilute particle flows through inclusion of a binary collision integral (O'Rourke, 1981) in the transport equation for the particle distribution function, but models based on just binary collisions are inappropriate for the dense particle flows of interest in this study, where n-body collisions with $n>2$ are important.

The situation in gas/liquid/solid fluidized beds is more complicated than in gas dynamics because, in addition to collisions causing particle velocities to relax to an equilibrium value, particle collisions cause transfer and mixing of liquid film mass and, consequently, result in equilibration of liquid film masses, chemical compositions, and film temperatures. To represent this situation, we assume that there are two BGK-like terms on the right-hand side of the particle distribution function, with different equilibrium distributions and different collisional time scales. One time scale is associated with achieving particle velocity equilibrium with other particle properties frozen, and the other time scale is associated with achieving full equilibration of film masses, velocities, compositions, and temperatures.

The two collision time scales are both proportional to the average time between collisions experienced by an individual particle. Our expression for the time between collisions is intended to apply for all particle concentrations, from the dilute to the close-packed particle limits. In the dilute particle limit, we use reasoning analogous to that used in the kinetic theory of dilute gases to derive a collision time scale. In the close-packed particle limit, our expression for the time between collisions properly goes to zero.

The two collision time scales of the BGK-like terms differ because of the differing effectiveness of collisions in bringing about particle velocity equilibrium and liquid film composition and thermal equilibrium. Collisions tend to bring about velocity equilibrium primarily because of the inelastic nature of particle collisions. Collisions between solid particles reduce the kinetic energy of relative motion because of the small solid deformations and energy dissipation that result from collisions. The energy dissipation in collisions is greatly enhanced when surface films are present because collisional forces cause liquid film motions and surface deformations, which lead to more energy dissipation than in the case of solid particle collisions. Collisions between particles with films can also lead to particle coalescence (O'Rourke, 1981), an effect that is ignored in this study.

In contrast to the above velocity equilibration mechanisms, collisional equilibration of the liquid film properties is primarily caused by the exchange, or transfer, of liquid mass between particles that occurs when particles collide. Collisional forces cause liquid to be moved between particles, and, if there is sufficient force in the collision, the liquid can splash and adhere to the surfaces of neighboring particles. Liquid transferred from one particle to another mixes with the liquid on its new particle, causing the liquid temperatures and compositions on colliding particles to be more nearly equal.

In this work, we assume that at equilibrium the ratio of the liquid to solid mass of individual wet particles is constant which is equal to the local ratio of the total liquid to total solid mass density. While it is intuitively clear that liquid film will migrate from particle to particle as a result of collisions, it is not clear what the equilibrium distribution of liquid film masses will be. It can easily be seen that our assumption is equivalent to the assumption that, at equilibrium, the ratio of the liquid film thickness to solid particle radius is locally a constant which is independent of solids radius. Thus, for example, a solid particle whose radius is twice that of another solid particle will have a liquid film that is twice as thick at equilibrium. A necessary condition for our assumption to be true is that inertial forces dominate over surface tension and viscous forces in the collisions, so that the equilibrium distribution of liquid mass over the surfaces of solid particles assumes a form that is independent of these liquid material properties. Our assumption contrasts with, and improves upon, the assumption made by some authors of a constant film thickness, independent of the radius of the solid particle upon which the film adheres (Song et al., 2004).

In our numerical method, integration of the collision terms is performed within the framework of the computational particle method used by MP-PIC (Andrews and O'Rourke, 1996; Snider et al., 1998; Snider, 2001). In the MP-PIC method, the continuous distribution function of particle properties, which is obtained by a turbulence averaging procedure, is numerically approximated by a discrete distribution of Lagrangian computational parcels, each of which represents a number of physical particles with identical properties. In this study, we take the properties of physical particles to be their location, solid mass, the masses of the chemical species in their liquid film, particle velocity, solid temperature, and liquid film temperature. We assume that the temperature and chemical composition within each particle's film is uniform, but that the film temperature can differ from the solid particle temperature.

In our numerical method for integrating the collision terms, because of computer memory limitations we keep the same computational parcels, with the same number of physical particles in each parcel, but update the particle properties associated with these parcels. The numerical calculation of collision effects is done on a cell-by-cell basis and is split from the calculation of other particle property changes. We determine the new parcel properties by using an implicit approximation to the collision equations to obtain a provisional discrete distribution in which parcel numbers are increased. Then, we "numerically" agglomerate parcels in the provisional distribution into the new parcels in such a way that particle mass, momentum, and energy are conserved.

The MP-PIC method is used for calculating particle dynamics in the general purpose computational-particle fluid dynamics (CPFD) numerical methodology. The CPFD numerical methodology is incorporated in the commercial Barracuda® code, which is the platform for implementing the collision model in this paper.

The remainder of this paper is organized as follows. In the next section, we give the equations of the extended MP-PIC method that involve the new collision terms. A particle distribution function for gas/liquid/solid fluidized beds is defined, the transport equation for this distribution function is given, and the two equilibrium distributions and collisional time scales discussed above are specified. In Section 3, we demonstrate several properties of the collision terms, including the fact that they conserve the mass, momentum, and enthalpy of the particle phase. Next, we document the numerical method used to integrate the collision terms. In the final section, we present examples of fluidized bed calculations using the new collision model, including calculations of gas/solid and gas/liquid/solid beds.

2. MP-PIC equations with collisions

The dynamics of the particle field is obtained in the MP-PIC method by solving for the particle distribution function f. In this section we define f and give its transport equation with the new BGK-like collision terms. To define the collision terms, which are the main subject of this paper, we must specify two equilibrium particle distributions and the relaxation times corresponding to these distributions. Considerable time is spent in this section presenting and motivating the expressions we use for these collision quantities.

The distribution function f is the local number density of particles times the local probability distribution function of particle properties that are important in our particular application. For gas/liquid/solid fluidized beds, we take as particle properties the mass of the solid part of the particle M_s; the masses of each of the chemical components i in the liquid film on a particle $M_{f,i}$; the particle velocity u_j; the temperature of the solid part of the particle T_s; and the

temperature of its film part T_f. Thus,

$$f(x_j, M_s, M_{f,i}, u_j, T_s, T_f, t)\,\mathrm{d}M_s\,\mathrm{d}M_{f,i}\,\mathrm{d}u_j\,\mathrm{d}T_s\,\mathrm{d}T_f$$

is the average number density of particles at spatial location x_j and at time t, with solid mass in the interval $(M_s, M_s + \mathrm{d}M_s)$, mass of liquid species i in the interval $(M_{f,i}, M_{f,i} + \mathrm{d}M_{f,i})$, Cartesian velocity component j in the interval $(u_j, u_j + \mathrm{d}u_j)$, solid temperature in the interval $(T_s, T_s + \mathrm{d}T_s)$, and liquid temperature in the interval $(T_f, T_f + \mathrm{d}T_f)$. When an alphabetic letter is used as a subscript in this paper, it is understood, unless noted otherwise, that the letter runs over all its possible values. Thus, $\mathrm{d}u_j$ represents $\mathrm{d}u_1\mathrm{d}u_2\mathrm{d}u_3$, and $M_{f,i}$ represents $M_{f,1}, M_{f,2}, \ldots, M_{f,NS}$, where NS is the number of chemical species in the liquid film. For brevity in what follows, we often denote by ϕ_j those independent variables of the distribution function f exclusive of spatial location x_j and time t. Thus, the above expression will often be written as

$$f(x_j, M_s, M_{f,i}, u_j, T_s, T_f, t)\,\mathrm{d}M_s\,\mathrm{d}M_{f,i}\,\mathrm{d}u_j\,\mathrm{d}T_s\,\mathrm{d}T_f = f(x_j, \phi_j, t)\,\mathrm{d}\phi_j. \tag{1}$$

With NS chemical species in the liquid film, the number of independent variables represented by ϕ_j in Eq. (1) is $NS + 6$.

The transport equation for the particle distribution function is

$$\frac{\partial f}{\partial t} + \frac{\partial (f u_j)}{\partial x_j} + \frac{\partial (f \dot{\phi}_j)}{\partial \phi_j} = \frac{f^{eq,u} - f}{\tau^u} + \frac{f^{eq,t} - f}{\tau^t}. \tag{2}$$

Eq. (2) is derived in an analogous fashion to the derivation of the Boltzmann equation of gas dynamics (Vincenti and Kruger, 1975). For each k, the quantity $\dot{\phi}_k(x_j, \phi_j, t)$ is the time rate of change of the value of ϕ_k of a particle located at x_j with properties ϕ_j at time t. Specification of $\dot{\phi}_k$ does not concern us in this study, but will be the subject of a future paper documenting our model for gas/liquid/solid fluidized beds. See Andrews and O'Rourke (1996) for an example of an expression for $\dot{u}_j$ that includes the effects of drag due to particle motion relative to the continuous gas phase, buoyant forces, gravitational acceleration, and an isotropic inter-particle stress.

The right-hand side of Eq. (2) represents the time rate of change of f due to particle collisions and is denoted by $(\partial f/\partial t)_{coll}$:

$$\left(\frac{\partial f}{\partial t}\right)_{coll} = \frac{f^{eq,u} - f}{\tau^u} + \frac{f^{eq,t} - f}{\tau^t}. \tag{3}$$

Specification of collision effects in our model requires the definition of two equilibrium distributions $f^{eq,u}$ and $f^{eq,t}$ and two collision time scales τ^u and τ^t, and we now define these quantities. The equilibrium distribution $f^{eq,u}$ is the distribution that results if particle velocities are equilibrated, and the remainder of the particle distribution remains unchanged. Its definition uses the local mass-averaged velocity $u_{j,eq}$, which is defined by

$$u_{j,eq} = \frac{\int f M_p u_j\,\mathrm{d}\phi_k}{\int f M_p\,\mathrm{d}\phi_k} \quad \text{for each } j, \tag{4}$$

where the total particle mass M_p includes its solid mass and its liquid film mass:

$$M_p = M_s + \sum_{i=1}^{NS} M_{f,i}. \tag{5}$$

The integrals in Eq. (4) are over all variables ϕ_k and all values of those variables. In terms of $u_{j,eq}$, $f^{eq,u}$ is defined by

$$f^{eq,u} = \left[\int f\,\mathrm{d}u_j\right]\delta(u_j - u_{j,eq}). \tag{6}$$

In Eq. (6), the integral is over all values of all particle velocity components, and δ is the Dirac delta function. We also note our convention that the product of three δ functions is implied in Eq. (6).

The full distribution function $f^{eq,t}$ is the particle distribution that results when full collisional equilibrium of all particle quantities is achieved:

$$f^{eq,t} = \left[\int f\,\mathrm{d}M_{f,i}\,\mathrm{d}u_j\,\mathrm{d}T_f\right]\delta(M_{f,i} - \lambda_i M_s)\delta(u_j - u_{j,eq})\delta(T_f - T_{f,eq}). \tag{7}$$

Collisions do not affect the solid masses or temperatures. In Eq. (7), λ_i is the local ratio of the mass of liquid species i to the solids mass:

$$\lambda_i = \frac{\int f M_{f,i}\,\mathrm{d}\phi_j}{\int f M_s\,\mathrm{d}\phi_j} \quad \text{for each } i. \tag{8}$$

The quantity $T_{f,eq}$ is the equilibrium temperature that would result if all the liquid at point x_j at time t were mixed at constant pressure; $T_{f,eq}$ is implicitly determined by the equation

$$\int f \sum_{i=1}^{NS} M_{f,i} h_i(T_f)\,\mathrm{d}\phi_j = \sum_{i=1}^{NS} h_i(T_{f,eq}) \int f M_{f,i}\,\mathrm{d}\phi_j, \tag{9}$$

where h_i is the mass-specific enthalpy of liquid species i.

Eqs. (7) and (8) show that at equilibrium we are assuming that each particle has the same ratio of mass of liquid film species i to solids mass, and this assumption requires some comment. Define quantity λ by

$$\lambda = \sum_{i=1}^{NS} \lambda_i. \tag{10}$$

From Eqs. (8) and (10), λ is the local ratio of total liquid mass to solid mass. It is seen from Eq. (7) that we are assuming that, at equilibrium, the mass fraction of liquid species i is the same for each particle and is equal to λ_i/λ. This assumption is consistent with our physical picture that collisions cause mixing of the liquid films on different particles.

Our model also requires, however, that we make an additional assumption regarding the distribution of liquid mass on the solid particles at equilibrium. It is seen from Eqs. (7) and (8) that we are assuming that at equilibrium, the ratio of total liquid to solid mass is the same for each particle. While it is not clear how accurate this assumption is, it is a simple assumption that is consistent with a physical picture that liquid dynamics during collisions is inertially dominated, and surface tension and viscous forces do not play a role.

We now turn to the definition of the collision times τ^u and τ^t. These are defined as being proportional to a time between collisions τ_{coll}:

$$\tau^u = \tau_{coll}/K_u \tag{11}$$

and

$$\tau^t = \tau_{coll}/K_t, \tag{12}$$

where K_u and K_t are positive dimensionless factors that may be functions of local mean particle properties. In this study, we take K_u and K_t to be functions of λ. (See Eq. (61).) Physically, K_u and K_t specify the efficiency of collisions in bringing about equilibrium, with lower values of these constants corresponding to larger equilibration times.

The time between collisions τ_{coll} is given by

$$\frac{1}{\tau_{coll}} = \frac{u'_{rms}}{r_{32}} \frac{\theta_{cp}\theta_p}{\theta_{cp} - \theta_p}. \tag{13}$$

In Eq. (13), u'_{rms} is the mass-weighted root-mean-square velocity fluctuation,

$$u'_{rms} = \left[\frac{\int f M_p (u_j - u_{j,eq})^2\,\mathrm{d}\phi_k}{\int f M_p\,\mathrm{d}\phi_k}\right]^{1/2}, \tag{14}$$

where $u_{j,eq}$ is defined in Eq. (4) and M_p in Eq. (5). The quantity θ_p in Eq. (13) is the particle-phase volume fraction:

$$\theta_p = \int f V_p \, \mathrm{d}\phi_j. \tag{15}$$

The volume of a single particle is

$$V_p = \frac{M_s}{\rho_s} + \frac{\sum_i M_{f,i}}{\rho_f}, \tag{16}$$

where ρ_s is the solid density which may be a function of T_s, and ρ_f is the liquid density which may be a function of T_f and the mass fractions of the liquid chemical species. The quantity θ_{cp} is the close-pack volume fraction of the particle phase. For the present case of particles composed of both solid cores and liquid films, we use the expression

$$\theta_{cp} = \min\left[\theta_{cp,s}\frac{\theta_p}{\theta_s}, 1\right], \tag{17}$$

where θ_s is the solid-phase volume fraction

$$\theta_s = \int f \frac{M_s}{\rho_s} \, \mathrm{d}\phi_j \tag{18}$$

and $\theta_{cp,s} < 1$ is the known close-pack volume fraction when the particle phase is composed of pure solids ($\theta_p = \theta_s$).

The Sauter mean radius (Fan and Zhu, 1998) of the particle distribution is defined as

$$r_{32} = \frac{\int f r^3 \, \mathrm{d}\phi_j}{\int f r^2 \, \mathrm{d}\phi_j}, \tag{19}$$

where r is the effective particle radius, $r = (V_p/4/3\pi)^{1/3}$. The Sauter mean radius is the radius of the distribution of equal-sized particles with the same volume and surface area as the distribution f.

We now give justification for Eq. (13) specifying the time between collisions. In part, Eq. (13) is motivated by an expression for the binary collision frequency of equal-sized molecules in a billiard-ball model for dilute gases (Vincenti and Kruger, 1975). This collision frequency is shown to be

$$\frac{1}{t_{coll}} = u_{rel} 4\sqrt{2}\pi r^2 N, \tag{20}$$

where u_{rel} is the average relative velocity between molecules, r is the molecule radius, and N is the number density of molecules. By using the relation $\theta_p = \frac{4}{3}\pi r^3 N$ to eliminate the number density in favor of θ_p in Eq. (20), one obtains

$$\frac{1}{t_{coll}} = 3\sqrt{2}\frac{u_{rel}}{r}\theta_p. \tag{21}$$

Eq. (21) agrees with Eq. (13) in the dilute particle limit if u_{rel} is replaced by u'_{rms} and r is replaced by r_{32}. For high volume fraction particle flows, the time between collisions in Eq. (13) is modified so that t_{coll} goes to zero as the particle volume fraction approaches the close-pack limit.

3. Properties of the particle collision terms

We now demonstrate some properties of the new collision terms. First, we show that, consistent with the physics of particle collisions, particle mass, momentum, and enthalpy are conserved by the collision terms. Because particle collisions are inelastic, the fluctuational kinetic energy of the particle field is not conserved, and we next derive an equation for the decay rate of fluctuational kinetic energy due to collisions. Finally, we present an analytic solution of the collision equations. This solution shows that if there is collisional equilibrium, then the particle distribution function f is equal to the full equilibrium distribution $f^{eq,t}$ defined in Eq. (7).

Particle mass, momentum, and enthalpy are conserved by the new collision terms if the following conditions are satisfied:

$$\int \left(\frac{\partial f}{\partial t}\right)_{coll} M_s \, \mathrm{d}\phi_k = 0, \tag{22}$$

$$\int \left(\frac{\partial f}{\partial t}\right)_{coll} M_{f,i} \, \mathrm{d}\phi_k = 0 \quad \text{for each } i, \tag{23}$$

$$\int \left(\frac{\partial f}{\partial t}\right)_{coll} M_p u_j \, \mathrm{d}\phi_k = 0 \quad \text{for each } j \quad \text{and} \tag{24}$$

$$\int \left(\frac{\partial f}{\partial t}\right)_{coll} \left(M_s h_s(T_s) + \sum_i M_{f,i} h_i(T_f)\right) \mathrm{d}\phi_k = 0. \tag{25}$$

The quantity $(\partial f/\partial t)_{coll}$ is defined in Eq. (3). Eqs. (22), (23), (24), and (25) are statements that the time-rate of change due to collisions of solid mass, the mass of liquid species i, momentum in the j-coordinate direction, and enthalpy, respectively, are conserved in particle collisions. Satisfaction of these conditions ensures that collision terms do not appear in conservation equations for mass, momentum, and enthalpy for the particle phase (Andrews and O'Rourke, 1996).

To demonstrate that Eqs. (22)–(25) are true, we first substitute for $(\partial f/\partial t)_{coll}$ in these equations using Eq. (3). The collision times τ^u and τ^t can be brought outside the integrals over ϕ_k since their defining equations, Eqs. (11)–(19), show that these collision times depend only on x_j and time t, and not on any of the coordinates in ϕ_k. It is thus seen that it is sufficient to show that the equilibrium distributions $f^{eq,u}$ and $f^{eq,t}$ have the same mass, momentum, and enthalpy as the original distribution f.

As an example, we now demonstrate that $f^{eq,u}$ has the same momentum in the j-coordinate direction as f. The demonstrations of the other assertions follow similarly. By using the definition of $f^{eq,u}$ in Eq. (6), we obtain

$$\int f^{eq,u} M_p u_j \, \mathrm{d}\phi_k = \int \left[\int f \, \mathrm{d}u_l\right] \delta(u_l - u_{l,eq}) M_p u_j \, \mathrm{d}\phi_k \quad \text{for each } j. \tag{26}$$

We now perform the integrations over the velocity coordinates in ϕ_k on the right-hand side of Eq. (26) and use the substitution property of the δ-function, to obtain

$$\int f^{eq,u} M_p u_j \, \mathrm{d}\phi_k = \int \left[\int f \, \mathrm{d}u_l\right] M_p u_{j,eq} \, \mathrm{d}M_s \, \mathrm{d}M_{f,i} \, \mathrm{d}T_s \, \mathrm{d}T_f. \tag{27}$$

The integrations over u_l in the inner integral on the right-hand side of Eq. (27) may be moved outside all terms in the integrand since, with the exception of f, these terms do not depend on u_l:

$$\int f^{eq,u} M_p u_j \, \mathrm{d}\phi_k = \int f M_p u_{j,eq} \, \mathrm{d}\phi_k. \tag{28}$$

Finally, we substitute for $u_{j,eq}$ in the right-hand side of Eq. (28), from its definition in Eq. (4), to obtain

$$\int f^{eq,u} M_p u_j \, \mathrm{d}\phi_k = \int f M_p u_j \, \mathrm{d}\phi_k. \tag{29}$$

This shows that the distributions f and $f^{eq,u}$ have the same particle momentum.

We now indicate how one may derive an equation for the time rate of change due to collisions of the fluctuational kinetic energy of the particle field. This equation relates the time scale of the decay of fluctuational kinetic energy to the collision times τ^u and τ^t, and provides some guidance in the choice of these collisional times. The fluctuational kinetic energy k of the particle field, which is proportional to the so-called granular temperature (Lun et al., 1984), is defined by

$$k = \tfrac{1}{2}(u'_{rms})^2, \tag{30}$$

where u'_{rms} is defined in Eq. (14). We want to derive an equation for $\partial k/\partial t = (\partial k/\partial t)_{coll}$ when $\partial f/\partial t = (\partial f/\partial t)_{coll}$. First, it is easy to see that

$$\frac{\partial}{\partial t}\int f M_p \, \mathrm{d}\phi_j = 0 \quad \text{when} \quad \frac{\partial f}{\partial t} = \left(\frac{\partial f}{\partial t}\right)_{coll}. \tag{31}$$

To prove Eq. (31), one brings the time-derivative inside the integral, and uses Eqs. (5), (22), and (23). Next, one shows that

$$\int f^{eq,u} M_p (u_j - u_{j,eq})^2 \, \mathrm{d}\phi_k = \int f^{eq,t} M_p (u_j - u_{j,eq})^2 \, \mathrm{d}\phi_k = 0 \tag{32}$$

by using the defining equations for $f^{eq,u}$ and $f^{eq,t}$ and integrating over the velocity coordinates in ϕ_k. Then, by using the defining equations for k, Eqs. (30) and (14), bringing the time-derivative in the resulting equation inside the integral, and using the definition of $(\partial f/\partial t)_{coll}$ in Eqs. (3), (31) and (32), one can derive

$$\left(\frac{\partial k}{\partial t}\right)_{coll} = -k\left(\frac{1}{\tau^u} + \frac{1}{\tau^t}\right). \tag{33}$$

Eq. (33) shows that the time scale for collisional decay of the width of the velocity distribution is $\tau^u\tau^t/(\tau^u + \tau^t)$.

Similarly, if one defines the width of the mass distribution of liquid species i by

$$\sigma_M^2 = \int f(M_{f,i} - \lambda_i M_s)^2 \, \mathrm{d}\phi_k, \tag{34}$$

it can be shown that when $\mathrm{d}f/\mathrm{d}t = (\mathrm{d}f/\mathrm{d}t)_{coll}$,

$$\frac{\mathrm{d}\sigma_M^2}{\mathrm{d}t} = -\frac{\sigma_M^2}{\tau^t}. \tag{35}$$

Thus, τ^t is the time scale for collisional decay in the width of the mass distributions of the liquid species. Eqs. (33) and (35) show that the ratio R of the time scale for decay of liquid mass fluctuations, to the time scale for decay of particle velocity fluctuations, is

$$R = \frac{\tau^u + \tau^t}{\tau^u} = \frac{K_u + K_t}{K_t}, \tag{36}$$

where K_u and K_t are defined in Eqs. (11) and (12).

Eq. (36) can help guide us in postulating expressions for K_u and K_t. For example, if, as discussed in the introduction to this paper, we expect that equilibration of liquid film masses occurs on a longer time scale than equilibration of particle velocities, then this implies that $K_u > 0$.

Finally, we show that if there is collisional equilibrium, then $f = f^{eq,t}$. We note that it is not immediately clear that this equilibrium condition is satisfied. By "collisional equilibrium," we mean that

$$\frac{\partial f}{\partial t} = \left(\frac{\partial f}{\partial t}\right)_{coll} = 0 \quad \text{(collisional equilibrium condition)}. \tag{37}$$

By using the definition of $(\partial f/\partial t)_{coll}$, Eq. (3), in Eq. (37), and solving for f, one obtains

$$f = \frac{f^{eq,u}/\tau^u + f^{eq,t}/\tau^t}{1/\tau^u + 1/\tau^t}, \tag{38}$$

when there is collisional equilibrium. It appears that Eq. (38) implies f may not equal $f^{eq,t}$ since, in general, $f^{eq,u} \neq f^{eq,t}$. The fact that f satisfies Eq. (38), however, does imply $f = f^{eq,t}$, as we now show. First, one can easily show using Eqs. (6) and (7) and properties of the δ-function that

$$(f^{eq,u})^{eq,u} = f^{eq,u} \quad \text{and} \quad (f^{eq,t})^{eq,u} = f^{eq,t}. \tag{39}$$

By applying the $(\,)^{eq,u}$-operator to each side of Eq. (38) and using Eq. (39), one can show that $f^{eq,u} = f^{eq,t}$ and, hence that $f = f^{eq,t}$ when there is collisional equilibrium.

4. Numerical method for integrating the collision terms

We now describe the numerical method for integrating the collision terms. This particle numerical method is incorporated into the framework of the MP-PIC method (Andrews and O'Rourke, 1996; Snider et al., 1998; Snider, 2001), and included within the CPFD numerical methodology in the commercial Barracuda code. We first give a brief overview of the MP-PIC method. We then detail the numerical integration of the collision terms. Finally, we show that the particle velocities that result from the collision calculation are, in a sense, well-behaved if the collision constants K_u and K_t, defined in Eqs. (11) and (12) are positive.

In the MP-PIC method, the continuous particle distribution function f is approximated by a discrete distribution f_d of computational parcels. Each computational parcel p represents a number N_p of physical particles with identical location $x_{j,p}$ and other particle properties $\phi_{j,p}$; thus,

$$f(x_j, \phi_j, t) \approx f_d(x_j, \phi_j, t) = \sum_p N_p \delta(x_j - x_{j,p})\delta(\phi_j - \phi_{j,p}), \tag{40}$$

where the sum is over all particles in the computational domain. The time evolution of the parcel locations $x_{j,p}$ and other properties $\phi_{j,p}$ is obtained by numerical solution of the ordinary differential equations $\mathrm{d}x_{j,p}/\mathrm{d}t = u_{j,p}$ and $\mathrm{d}\phi_{j,p}/\mathrm{d}t = \dot{\phi}_j(x_{k,p}, \phi_{k,p}, t)$, where the parcel velocities $u_{j,p}$ are among the properties $\phi_{j,p}$ and the $\dot{\phi}_j$ are prescribed functions of the spatial locations, the other particle properties, and time. The space and time dependence of the functions $\dot{\phi}_j$ are introduced primarily through their dependence on the space- and time-dependent properties of the continuous phase in which the particles are embedded. Numerical solution for the continuous phase is by a time-marching, conservative finite volume method. Communication between the particle-phase and continuous-phase numerical solutions is accomplished through interpolation functions $S_\xi(x_j)$, where the subscript refers to a computational cell ξ in the finite difference grid. Thus, for example, the value of continuous phase property Q at the location of particle p, denoted by Q_p, is given by

$$Q_p = \sum_\xi S_\xi(x_{j,p}) Q_\xi, \tag{41}$$

where Q_ξ is the computed value of Q in computational cell ξ. These interpolation functions are also used in calculating source terms to the continuous phase due to mass, momentum, and energy exchange with the particle phase. Source term interpolation is done in such a way that the mass, momentum, and energy of the combined continuous/particle-phase flow are numerically conserved. The MP-PIC method is an extension of the so-called stochastic parcel method for dispersed particle flows (O'Rourke, 1981; Dukowicz, 1980;

Amsden et al., 1989) to flows in which the particles may occupy volume fractions up to the close-pack limit.

The strengths of the MP-PIC method are its abilities to simulate dense particle flows and to include efficiently the effects of a distribution of particle properties, and its numerical accuracy due to the Lagrangian nature (Dukowicz, 1980) of its numerical solution procedure for the particle phase.

We now turn to the numerical method for integrating the BGK-like collision terms within the framework of the MP-PIC method. The calculation of collisions is split from that of the remainder of the terms in the transport equation, Eq. (1), for the particle distribution function f. Thus, we are concerned with approximating the following equation for f:

$$\frac{\partial f}{\partial t} = \frac{f^{eq,u} - f}{\tau^u} + \frac{f^{eq,t} - f}{\tau^t}. \tag{42}$$

We also use an equation for $f^{eq,u}$ that is obtained by applying the operator $(\,)^{eq,u}$ to Eq. (42) and using Eq. (39) and the fact that this operator and the time derivative commute:

$$\frac{\partial f^{eq,u}}{\partial t} = \frac{f^{eq,t} - f^{eq,u}}{\tau^t}. \tag{43}$$

Eqs. (42) and (43) are approximated in each cell ξ of the computational mesh. The local discrete distribution $f^n_{d,\xi}$ in cell ξ is defined by

$$f^n_{d,\xi} = \sum_{p\in\xi} N_p \delta(x_j - x_{j,p})\delta(M_s - M_{s,p})\delta(M_{f,i} - M^n_{f,i,p}) \times \delta(u_j - u^n_{j,p})\delta(T_s - T_{s,p})\delta(T_f - T^n_{f,p}), \tag{44}$$

where the sum is over all particles located in cell ξ and the superscript n denotes the current, or "old-time," computed approximation to a particle property. The particle film masses, particle velocities, and particle film temperatures will be updated due to the collision calculation. The particle locations, solid masses, and solid temperatures do not have superscripts since their values do not change due to the collision calculation. We first calculate the cell values of the equilibrium velocities $u_{j,eq,\xi}$, the equilibrium mass ratios $\lambda_{i,\xi}$, particle film temperatures $T_{f,eq,\xi}$, and the collision times τ^u_ξ and τ^t_ξ, by using the local distribution $f^n_{d,\xi}$ in place of f in Eqs. (4), (8), (9), and (11)–(18) and integrating over the control volume of computational cell ξ in addition to all the other particle coordinates in these equations. The formulas for these quantities are easy to obtain, and we only give here, as an example, the formula for $u_{j,eq,\xi}$:

$$u_{j,eq,\xi} = \frac{\sum_{p\in\xi} N_p (M_{s,p} + \sum_i M^n_{f,i,p}) u^n_{j,p}}{\sum_{p\in\xi} N_p (M_{s,p} + \sum_i M^n_{f,i,p})}. \tag{45}$$

In terms of the equilibrium particle properties, the equilibrium distributions $f^{eq,u}_\xi$ and $f^{eq,t}_\xi$ in cell ξ are obtained by substituting the distribution $f^n_{d,\xi}$, Eq. (44), in place of f in Eqs. (6) and (7), respectively. Thus,

$$f^{eq,u}_\xi = \sum_{p\in\xi} N_p \delta(x_j - x_{j,p})\delta(M_s - M_{s,p})\delta(M_{f,i} - M^n_{f,i,p}) \times \delta(u_j - u_{j,eq,\xi})\delta(T_s - T_{s,p})\delta(T_f - T^n_{f,p}) \tag{46}$$

and

$$f^{eq,t}_\xi = \sum_{p\in\xi} N_p \delta(x_j - x_{j,p})\delta(M_s - M_{s,p})\delta(M_{f,i} - \lambda_{i,\xi} M_{s,p}) \times \delta(u_j - u_{j,eq,\xi})\delta(T_s - T_{s,p})\delta(T_f - T_{f,eq,\xi}). \tag{47}$$

Note that because of the definitions of the equilibrium properties, it is easily verified that the distributions $f^{eq,u}_\xi$ and $f^{eq,t}_\xi$ have the same film species masses, particle momentum, and film enthalpy, as the original distribution $f^n_{d,\xi}$.

To obtain our approximations for the new or advanced time values of the particle film masses $M^{n+1}_{f,i,p}$, particle velocities $u^{n+1}_{j,p}$, and particle film temperatures $T^{n+1}_{f,p}$, we first calculate provisional approximations $\tilde{f}^{eq,u}_\xi$ and $\tilde{f}_\xi$ to the advanced-time distributions $f^{eq,u}_\xi$ and $f^n_{d,\xi}$, respectively. These provisional distributions are obtained as solutions to the following linearly implicit approximations to Eqs. (42) and (43):

$$\frac{\tilde{f}_\xi - f^n_{d,\xi}}{\delta t} = \frac{\tilde{f}^{eq,u}_\xi - \tilde{f}_\xi}{\tau^u_\xi} + \frac{f^{eq,t}_\xi - \tilde{f}_\xi}{\tau^t_\xi} \tag{48}$$

and

$$\frac{\tilde{f}^{eq,u}_\xi - f^{eq,u}_\xi}{\delta t} = \frac{f^{eq,t}_\xi - \tilde{f}^{eq,u}_\xi}{\tau^t_\xi}, \tag{49}$$

where δt is the computational time step. One obtains an equation for $\tilde{f}_\xi$ in terms of known distributions $f^n_{d,\xi}$, $f^{eq,u}_\xi$, and $f^{eq,t}_\xi$ by first solving for $\tilde{f}^{eq,u}_\xi$ in terms of the known distributions $f^{eq,u}_\xi$ and $f^{eq,t}_\xi$ using Eq. (49), substituting the result for $\tilde{f}^{eq,u}_\xi$ into Eq. (48), and solving Eq. (48) for $\tilde{f}_\xi$. After some algebraic rearrangement, we obtain

$$\tilde{f}_\xi - f^{eq,t}_\xi = \frac{f^{eq,u}_\xi - f^{eq,t}_\xi}{1 + \delta t/\tau^t_\xi} + \frac{f^n_{d,\xi} - f^{eq,u}_\xi}{1 + \delta t/\tau^t_\xi + \delta t/\tau^u_\xi}. \tag{50}$$

We note again that since the distributions $f^{eq,u}_\xi$ and $f^{eq,t}_\xi$ have the same masses, momentum, and enthalpy as the distribution $f^n_{d,\xi}$, from Eq. (50) it is easily shown that $\tilde{f}_\xi$ has the same masses, momentum, and enthalpy as $f^n_{d,\xi}$. It is also clear from Eq. (50) that as the computational time step goes to infinity, the provisional distribution $\tilde{f}_\xi$ converges to the equilibrium distribution $f^{eq,t}_\xi$, in agreement with the long-time behavior of the exact solution.

It is impossible to implement numerically the solution in Eq. (50) in a straightforward fashion because the number of computational parcels would rapidly grow and computer memory limits would be exceeded. This is because the straightforward implementation would require us each time step to split each computational parcel into three parcels. To see this, we substitute for $f^n_{d,\xi}$, $f^{eq,u}_\xi$, and $f^{eq,t}_\xi$ in Eq. (50) their sums over parcels in Eqs. (44),(46), and (47), respectively. The result is

$$\tilde{f}_\xi = \sum_{p\in\xi} N_p \delta(x_j - x_{j,p})\delta(M_s - M_{s,p})\delta(T_s - T_{s,p})\Delta_p, \tag{51}$$

where

$$\begin{aligned}\Delta_p = {} & \psi^n_\xi \delta(M_{f,i} - M^n_{f,i,p})\delta(u_j - u^n_{j,p})\delta(T_f - T^n_{f,p}) \\ & + (1 - \psi^n_\xi - \psi^t_\xi)\delta(M_{f,i} - M^n_{f,i,p})\delta(u_j - u_{j,eq,\xi})\delta(T_f - T^n_{f,p}), \\ & + \psi^t_\xi \delta(M_{f,i} - \lambda_{i,\xi} M_{s,p})\delta(u_j - u_{j,eq,\xi})\delta(T_f - T_{f,eq,\xi})\end{aligned} \tag{52}$$

and

$$\psi^n_\xi = \frac{1}{1 + \delta t/\tau^u_\xi + \delta t/\tau^t_\xi} \tag{53}$$

and

$$\psi_\xi^t = \frac{\delta t/\tau_\xi^t}{1+\delta t/\tau_\xi^t}. \tag{54}$$

Thus, in $\tilde{f}_\xi$ each parcel of the old-time distribution is split into three: one with $\psi_\xi^n N_p$ particles, one with $\psi_\xi^t N_p$ particles, and one with $(1-\psi_\xi^n-\psi_\xi^t)N_p$ particles.

In place of using the provisional distribution $\tilde{f}_\xi$, we "numerically agglomerate" the three parcels in each summand of Eq. (51) in such a way that mass, momentum, and enthalpy are conserved. More precisely, we take the distribution $f_{d,\xi}^{n+1}$ to have the same form as that of $f_{d,\xi}^n$ in Eq. (44) with the same number of particles N_p in parcel p and with the particle film masses $M_{f,i,p}^{n+1}$, particle velocities $u_{j,p}^{n+1}$, and particle film temperatures $T_{f,p}^{n+1}$ determined by requiring that the film masses, particle momenta, and film enthalpies of each parcel of $f_{d,\xi}^{n+1}$ be equal to the sum of those of its corresponding three parcels in Eq. (51). Straightforward calculations give the following new parcel properties:

$$M_{f,i,p}^{n+1} = (1-\psi_\xi^t)M_{f,i,p}^n + \psi_\xi^t \lambda_{i,\xi} M_{s,p}, \tag{55}$$

$$\begin{aligned}\left(M_{s,p}+\sum_i M_{f,i,p}^{n+1}\right)u_{j,p}^{n+1} &= \psi_\xi^n\left(M_{s,p}+\sum_i M_{f,i,p}^n\right)u_{j,p}^n \\ &+(1-\psi_\xi^n-\psi_\xi^t)\left(M_{s,p}+\sum_i M_{f,i,p}^n\right)u_{j,eq,\xi}, \\ &+\psi_\xi^t\left(M_{s,p}+\sum_i \lambda_{i,\xi}M_{s,p}\right)u_{j,eq,\xi}\end{aligned} \tag{56}$$

and

$$\begin{aligned}\sum_i M_{f,i,p}^{n+1}h_i(T_{f,p}^{n+1}) &= (1-\psi_\xi^t)\sum_i M_{f,i,p}^n h_i(T_{f,p}^n) \\ &+\psi_\xi^t\sum_i \lambda_{i,\xi}M_{s,p}h_i(T_{f,eq,\xi}).\end{aligned} \tag{57}$$

A question arises concerning the accuracy of the above "numerical agglomeration" procedure. The numerical solution equation (51) to the collision equations with BGK-like collision terms involves the superposition of fractions of the old-time and the equilibrium distributions. If the collision times are assumed constant, one can derive an analytic solution to Eqs. (42) and (43) that reveals this same behavior. Our "numerical agglomeration" procedure does not take this path to equilibrium, but, instead, uses a single distribution of the form of Eq. (44) in which particle properties collapse to their equilibrium values. We argue, however, that the detailed path to equilibrium is not physically meaningful. It is only physically meaningful to converge to the equilibrium distribution on the specified time scales, and this is accomplished by our numerical approximation.

We conclude this section on the numerical method for calculating collisions by showing that the advanced-time values $M_{f,i,p}^{n+1}$, $u_{j,p}^{n+1}$, and $T_{f,p}^{n+1}$ specified by Eqs. (55)–(57) lie between their old-time and equilibrium values if the collision times τ_ξ^u and τ_ξ^t are both positive. From Eq. (54), if τ_ξ^t is positive, then $0<\psi_\xi^t<1$. Thus, Eq. (55) shows that $M_{f,i,p}^{n+1}$ is a positively weighted average of $M_{f,i,p}^n$ and the equilibrium value of the mass $\lambda_{i,\xi}M_{s,p}$ and, thus, lies between these values.

To show that $T_{f,p}^{n+1}$ lies between $T_{f,p}^n$ and $T_{f,eq,\xi}$, we regard the left-hand side of Eq. (57) as a function of film temperature; that is, define

$$F(T) = \sum_i M_{f,i,p}^{n+1}h_i(T). \tag{58}$$

Using Eqs. (55) and (57), $0<\psi_\xi^t<1$, and the fact that the species specific heats at constant pressure are positive, one can show that $F(T_{f,i,p}^{n+1})$ lies between $F(T_{f,i,p}^n)$ and $F(T_{f,eq,\xi})$, and, hence, that $T_{f,p}^{n+1}$ lies between $T_{f,p}^n$ and $T_{f,eq,\xi}$.

Finally, to show that $u_{j,p}^{n+1}$ lies between $u_{j,p}^n$ and $u_{j,eq,\xi}$, one can combine Eqs. (55) and (56) to obtain

$$u_{j,p}^{n+1} = au_{j,p}^n + (1-a)u_{j,eq,\xi}, \tag{59}$$

where

$$a = \frac{\psi_\xi^n(M_{s,p}+\sum_i M_{f,i,p}^n)}{M_{s,p}+\sum_i M_{f,i,p}^{n+1}}. \tag{60}$$

Using Eq. (60), the assumptions that τ_ξ^u and τ_ξ^t are both positive, and the definition of ψ_ξ^n in Eq. (53), one can readily show that $0<a<1$. It then follows from Eq. (59) that $u_{j,p}^{n+1}$ lies between $u_{j,p}^n$ and $u_{j,eq,\xi}$.

One characteristic of our model is that total equilibrium is never reached when decay to momentum equilibrium is achieved before collision-decay to total equilibrium. At momentum equilibrium, particles are all moving at the equilibrium velocity and there are no velocity "fluctuations" which lead to collisions and equilibration of other particle properties. One can imagine a group of particles moving together at a constant speed, and without differences in particle speeds there are no collisions and there would be no transfer of mass or energy associated with collision. The first example problem below, where a liquid is injected into dense particle flow, illustrates this behavior.

5. Example calculations

The above collision model has been implemented in the commercial Barracuda software code, which has been used to perform two sets of example calculations documented below. In commercial operations, it is common to inject liquid into a fluidized bed. However, because of the complex churning and cross flows in fluidized beds, it is difficult to assess the influence of collision parameters on fluidized-bed calculations. The first set of example calculations uses a simple solid–gas flow with solid or liquid injection to isolate and examine collision behavior. In the second set, liquid injection into a fluidized bed is predicted and results compared to experiment data.

6. Liquid and solid injection into dense flow in a channel

The example chosen in this section is isothermal gas–solid flow in the rectangular duct shown in Fig. 1. A uniform distribution of solids and air enters one end of the channel and exits at the other end. At the center of the channel entrance, either a liquid or solid particle jet is injected in the direction of flow. The channel is 60 cm long, 15 cm high and 9 cm wide. The example uses a grid cell size of 1.5 cm by 1 cm by 1 cm. The solid density is 1000 kg/m^3 and the dry-solid particles have a constant radius of 50 or 100 μm. The gas is air at 300 K and 103 kPa. The liquid is water at 300 K. The particle close-pack volume fraction is 0.58.

The collisional relaxation of the particle velocities and liquid film masses towards equilibrium values is governed by Eq. (2). The momentum and total relaxation times are proportional to the collision time given by Eq. (13). The mechanism of the equilibration, which involves momentum transfer and the flow of liquid film between colliding particles, is not directly modeled. As with the BGK model

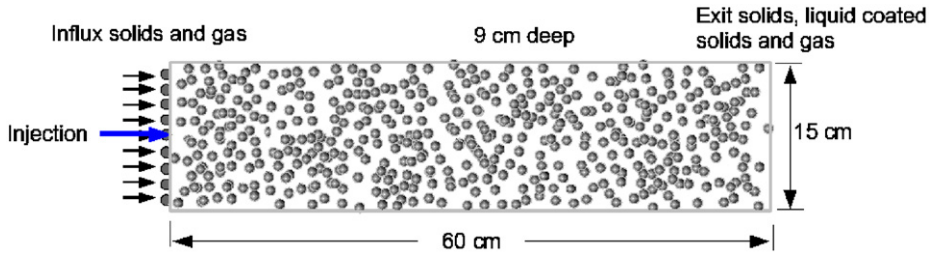

Fig. 1. Computational domain and boundary conditions. Inlet fluid flow with solid feed from the left and exit at a pressure boundary condition on the right. The long-arrow shows the injection direction in the center of the inlet face.

Table 1
Liquid and solid injection. Parameter variations indicated in boldface.

Case (type of injected particle)	Radii of feed and injected particles r_p (μm)	Particle feed volume fraction θ_p	Injection velocity U_{jet} (m/s)	Injection mass flow rate $\dot{m}$ (kg/s)
1 (liquid)	50	0.2	5	0.02
2 (liquid)	**100**	0.2	5	0.02
3 (liquid)	50	**0.4**	5	0.04
4 (liquid)	50	0.2	**10**	0.04
5 (**solid**)	50	0.2	5	0.02

of gas dynamics, the progress to an equilibrium state is governed by the relaxation time scales. The collision frequency depends on particle size, solids concentration and the magnitude of velocity fluctuations. The effects of these parameters and the different time scales for collisional momentum transfer and mass transfer are discussed in the examples below. In the calculations, dissipation of particle energy also occurs because of drag between particles and gas.

In calculations in the simple channel above, we explore the effects of several parameters on collisional relaxation to velocity and liquid-mass equilibrium. Four calculations of injection of liquid (Cases 1–4), and one calculation of injection of dry solids (Case 5), are listed with parameter variations indicated in boldface in Table 1. The liquid injection is implemented by using liquid on a very small solid core. The solid core radius is approximately 0.0001 μm, which results in a "liquid-particle". We note that in our model the liquid particles cannot deform or break up into new particles. The momentum and total collision equilibration time scales are proportional to the collision time as given by Eqs. (11) and (12). The ratio of time scales is given by Eq. (36) and is a constant $R = 4$ in all calculations. The rate coefficients are weighted by the ratio of local total liquid mass to total solid mass and the momentum and total equilibrium time scale coefficients are

$$K_{u,\xi} + K_{t,\xi} = \frac{K^S + \lambda_\xi K^L}{1 + \lambda_\xi}, \tag{61}$$

where ξ is a control volume and the constants are $K^S = 0.01$ and K^L=0.1, for pure solid (λ=0) and pure liquid (λ=∞), respectively. The sum of the rate coefficients is inversely proportional to the collisional relaxation time to velocity equilibrium. Thus, Eq. (61) prescribes that it takes about 100 collisions to achieve velocity equilibrium in a flow of pure solids and about 10 collisions to achieve velocity equilibrium in a flow of pure liquid droplets.

The variations in the four cases of liquid injection given in Table 1 provide a base for understanding the performance of collision mixing due to variations in key parameters. The calculations begin with stagnant air and no particles in the channel. Air and dry solids are then fed at a 1 m/s into the system as illustrated in Fig. 1. The solids are fed at a particle volume fraction of $\theta_p = 0.2$ in Cases 1, 2 and 4, which gives a bed velocity of 1.25 m/s. The feed volume fraction in Case 3 is $\theta_p = 0.4$ which gives a bed velocity of 1.67 m/s. After 0.5 s, when the gas and solids flow pattern has been established in the channel, the liquid-particle injection begins. The jet mass flux matches the bulk stream solid flux in Cases 1–3, but is twice the solid flux in Case 4. Fig. 2 shows the particle field for Case 1, which has dense particles flowing at a volume fraction of 0.2. Fig. 2 is a thin-slice of the three-dimensional space at the jet location. The solids are colored by their speed, where fast is red and slow is blue. From the figure, there is an expanding region of near constant velocity about the particle injection line where particles are moving near equilibrium velocity. While it is difficult to discern it from the figure, the jet region is very close to the free stream velocity at the end of the channel. The two particle fields shown in Fig. 2 are from a fine grid and a coarser grid. The coarse grid was used for the majority of calculations.

Fig. 3 shows velocities from Case 1 in which the liquid jet is injected at 5 m/s which is 5 times larger than the bulk solids flow velocity. Also shown in Fig. 3 are velocities from Case 4, in which the injection velocity is 10 m/s. All the velocity profiles in Fig. 3 are along the centerline of the jet. The bulk-mixture is dense solids flow with a particle volume fraction of 20%. While there is a significant concentration of solids, the solids are far from close pack, and the influence of particle concentration on collision frequency gives a multiplier on the order of one. The particle radius is small and will enhance collision mixing, but without local particle velocity fluctuations, the radius has no influence on collision frequency. At the jet nozzle, the calculated root-mean-square velocity fluctuation, U_{rms}, in Case 1 is approximately 1.5 m/s—which, in conjunction with the small particle sizes, gives a high collision frequency that drives the jet velocity to the equilibrium velocity within 10 cm. In Case 1, Fig. 4 shows the collision time, τ_{coll}, is 0.0002 s at the jet nozzle, and downstream, as the particles approach the equilibrium velocity, the collision time increases three orders of magnitude. At 10 cm from the entrance, the collision time is approximately 0.01 s, and for this collision time and a bulk stream velocity of 1.25 m/s, there are approximately 48 collisions before particles exit the channel. At 30 cm from the entrance, which is midway in the channel, the collision time is approximately 0.1 s, and for this collision time and a bulk flow of 1.25 m/s, there are only 4 or 5 collisions before a solid exits the channel. The slow decay towards equilibrium is expected the closer the velocity gets to the equilibrium velocity. (The equilibrium velocity is the local mass-averaged velocity of the combined liquid/solid phase.) If the injected velocity doubles, as in Case 4, collisions increase as seen in the collision time shown in Fig. 4. Both cases of particle injection at 5 and 10 m/s quickly go to equilibrium, and although there is more momentum in the higher velocity jet, both cases reach velocity equilibrium along the centerline of the jet at nearly the same location. As expected, Fig. 3 shows that, moving downstream, velocities along the jet path go to the local equilibrium velocity, and the fluctuation

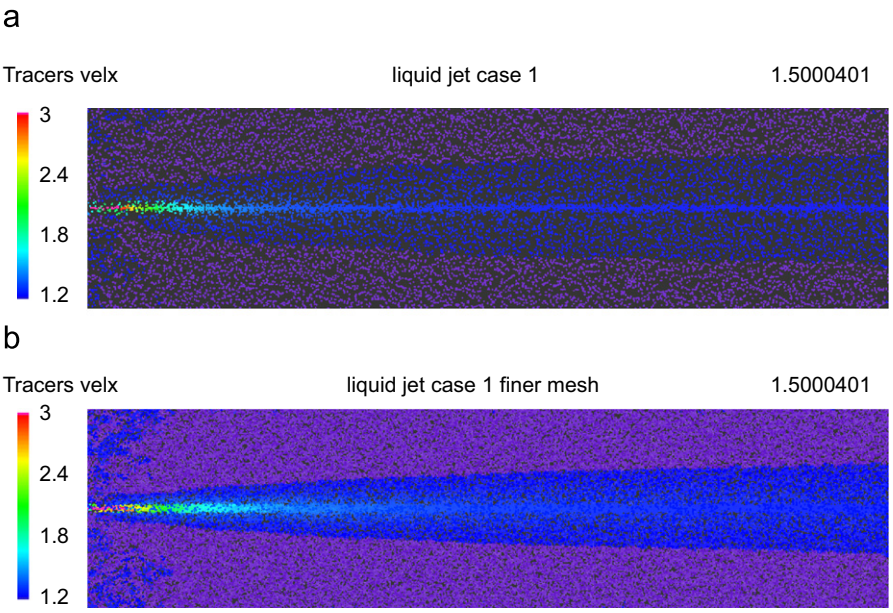

Fig. 2. Particle field in a thin slice through the jet axis in a three-dimensional dense particle flow field. Injection speed is 5 m/s and particle flow volume fraction is 0.2 (Case 1). (a) Grid cell size is 1.5 cm by 1 cm by 1 cm in the axial distance, vertical distance, and width distance, respectively. (b) Grid cell size is 0.8 cm by 0.6 cm by 0.6 cm in the axial distance, vertical distance, and width distance, respectively.

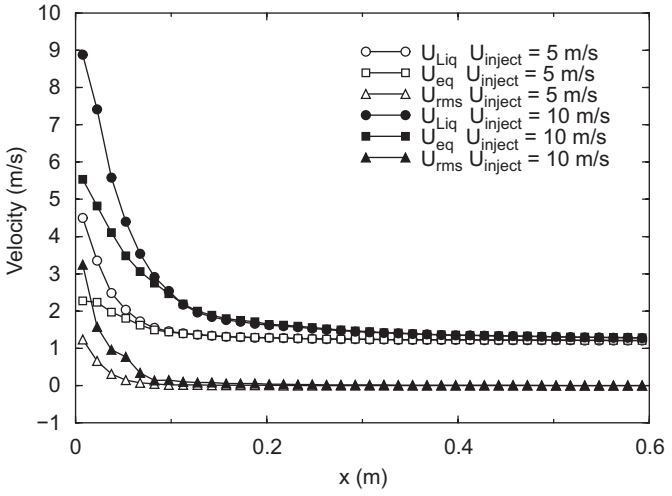

Fig. 3. Average liquid velocity U_{liq}, mass-averaged velocity of solids and liquid U_{eq}, and particle velocity fluctuation U_{rms} (see Eq. (14)) along the centerline of the jet in Cases 1 and 4 of Table 1.

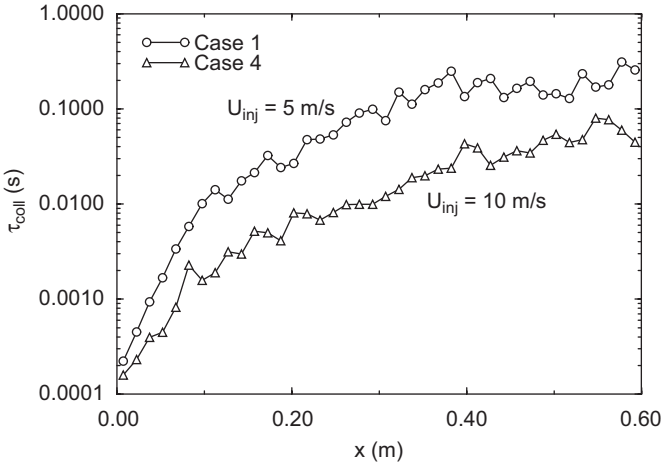

Fig. 4. The collision time along the injection path line for liquid injection in Cases 1 and 4. The injection rates are 5 and 10 m/s, the dense particle flow volume fraction is 0.2, and particles are 50 μm.

velocity becomes small. From Fig. 2, it is seen that there is a slight variation between bulk flow velocity and the expanding jet velocity, and global momentum equilibrium is not fully reached.

Note that there are two types of equilibrium to be considered here: the local velocity equilibrium of the liquid and solid particles spoken of above and the velocity equilibrium of the jet with the bulk flow exterior to the jet. Although the local velocities of solid and liquid equilibrate along the centerlines of the jets at nearly the same locations in Cases 1 and 4, from Fig. 3 the mass-averaged velocities of the liquid and solid particles do not equilibrate to the bulk-flow velocity until much farther downstream in Case 4, as one would expect for this higher momentum jet.

Fig. 5 compares the velocities for injection of liquid and injection of dry solids, Cases 1 and 5. The size, density and injection speed were the same for both solid and liquid injected particles. In the case for liquid injection, there is both liquid mass and momentum transfer between particles, while for dry solids injection, there is only momentum transfer between particles. As expected from the collision model, the liquid injected particles went to local momentum equilibrium faster than dry solids.

Fig. 7, comparing velocities in Cases 1 and 2, shows the rate of approach to momentum equilibrium decreases when the particle size is doubled. From Eq. (13), the collision time is linearly proportional to particle size, and one might expect that the time (distance downstream) to reach local momentum equilibrium would be about twice the time for particles with twice the size. Fig. 7 shows this doubling of time (distance) to local equilibrium happens; however, in general, this is not the case because of the complex interplay of solid–gas dynamics. Fig. 6 shows the collision time at distances down the channel. Near the jet, the collision time is shorter for smaller particles than larger particles, and smaller particles move toward velocity equilibrium faster than larger particles. Because the small particles quickly

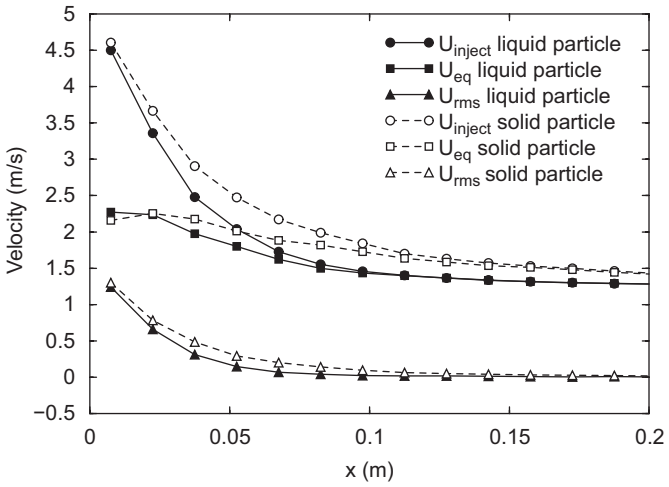

Fig. 5. Velocities of dry particles and liquid particle injection along the injection path line in Cases 1 and 5. The injection rates are 5 m/s, the dense particle flow volume fraction is 0.2, and particles are 100 μm.

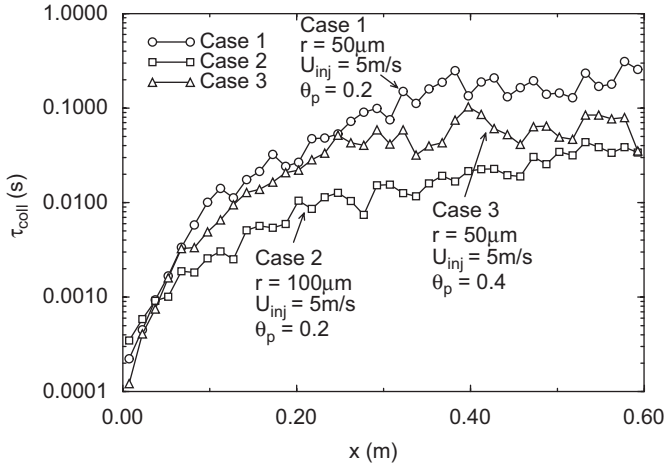

Fig. 6. Collision times for liquid particle injection along the injection path line.

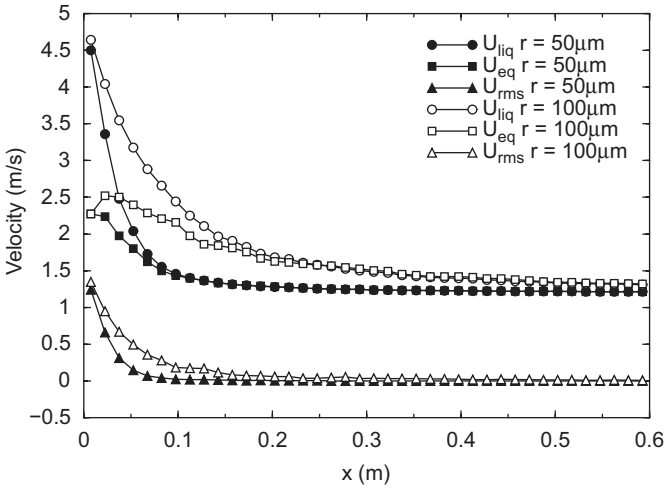

Fig. 7. Average liquid velocity U_{liq}, mass-averaged velocity of solids and liquid U_{eq}, and particle velocity fluctuation U_{rms} (see Eq. (14)) along the centerline of the jet in Cases 1 and 2 of Table 1.

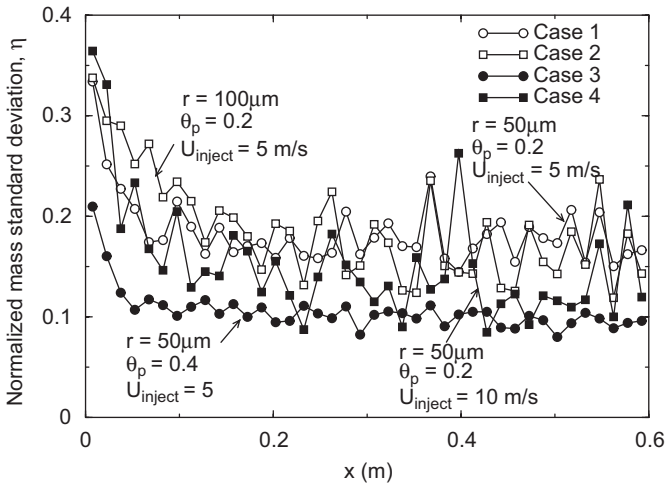

Fig. 8. The normalized standard deviation (see Eq. (34)) of the liquid mass distribution from the equilibrium mass distribution along the injection path line. Total equilibrium is at a value of zero.

approach velocity equilibrium, the velocity fluctuations quickly go to zero. On the other hand, larger particles have a prolonged time to velocity equilibrium, which gives prolonged larger velocity fluctuations, and the collision time curves cross in Fig. 6. Fig. 7 shows that the larger particles reach local velocity equilibrium within 20 cm along the injection path, but do not reach velocity equilibrium with the bulk flow before the particles exit the calculation domain.

In Case 3, bulk flow solids were fed at 40% volume fraction. Because this is far from close pack, there is only a small change from Case 1, which used 20% volume fraction. The increased particle volume fraction is seen in the collision time shown in Fig. 6. As particles go to close pack, the collision frequency goes to infinity and equilibrium will instantly be reached (see Eq. (13)). This is a logical picture that particles inter-connected at the maximum compaction will move as a solid body. While particle slipping and slight rearranging at close pack may occur, for the most part, the packed particles will move as a unit. The close-pack state is not limited to static piles of granular material. In fluidized beds and other particle-flow systems, particles collapse to close pack and re-fluidize.

The prior discussion focused on decay toward momentum equilibrium. The particles also move toward total equilibrium. In this isothermal case, total equilibrium is both mass and momentum equilibrium. Liquid particles are injected into the stream of dry particles and through collisions, liquid mass is transferred between particles. Fig. 8 shows the standard deviation, σ_M, of the liquid mass distribution from its equilibrium distribution as given by Eq. (34), normalized by the total liquid mass in a control volume

$$\eta_\xi = \frac{[\sum_{p\in\xi} N_p (M_f - \lambda_\xi M_s)^2]^{1/2}}{\sum_{p\in\xi} N_p M_f}. \tag{62}$$

The liquid mass distribution moves toward the total equilibrium value of zero. The particles leaving the jet for Cases 1–4 are liquid particles, and liquid is rapidly transferred between liquid particles and dry or partially wetted particles in the vicinity of the jet. Fig. 8 shows that within the first 10 cm from the jet orifice, the normalized standard deviation drops significantly, and after 10 cm, little liquid is transferred between particles. Fluctuations in the curves in Fig. 8 are a characteristic of stochastic flow of both dry and wet particles. The slow decay to total equilibrium is seen in the particles approaching momentum equilibrium (Figs. 3, 5 and 7) and the increase in collision time by two orders of magnitude in the first 10 cm from the jet (Figs. 4 and 6). In the collision model, total equilibrium cannot be attained if momentum equilibrium is achieved before total equilibrium is achieved.

Table 2
Experimental and Barracuda simulation parameters for liquid injection into a fluidized bed.

	Ariyapadi et al. (2003) (Section I)	Barracuda simulation
Bed dimensions	$20 \times 20 \times 100$ cm	$20 \times 20 \times 65$ cm
Solid particle density	(FCC) 1500 kg/m^3	1500 kg/m^3
Solid particle size distribution	Standard FCC (Sauter mean diameter $\sim 70\,\mu$m)	Standard FCC
Bed inventory	~ 9 kg	9.3 kg
Expanded bed height	~ 40 cm	~ 40 cm
Injected liquid	Ethanol (95% v/v)	Ethanol
Density of injected liquid	~ 800 kg/m^3	800 kg/m^3
Nozzle diameter	0.82 mm	Point source injection
Liquid droplet diameter	Not reported	0.42 mm
Injection time	10 s	10 s
Fluidization gas/conditions	Air at ambient conditions	Air at ambient conditions
K^S	N/A	0.01
K^L	N/A	0.1
Time scale ratio, R	N/A	4

Table 3
Liquid jet parameters for *Tests L* 1 and *L* 3 by Ariyapadi et al. (2003).

	Test L 1	*Test L* 3
Liquid mass flow rate (g/s)	2.9	6.0
Jet speed (m/s)	6.6	13.9
Fluidizing gas velocity (cm/s)	5.6	4.2

7. Liquid injection into a fluidized bed

Liquid is often injected into a fluidized bed or other solid–gas systems. Cokers are a good example where liquid hydrocarbon is sprayed into a hot fluidized bed of coke. The large surface area of solids provides for rapid vaporization and chemical reactions. Collisions between the liquid jet and solids spread liquid over the particles, and collisions between wet particles spread the liquid through the bed. As discussed previously in the description of the collision model, the collisions result in mass, momentum, and energy transfer between particles. This section applies the collision model to injection of liquid into an isothermal fluidized bed. The collision model is integrated into the CPFD software in the commercial code Barracuda.

The liquid injection experiment by Ariyapadi et al. (2003) is simulated by the fluidized bed calculations. Ariyapadi et al. (2003) used a non-intrusive X-ray imaging technique to investigate the horizontal injection of liquid and gas–liquid jets into a gas–solids fluidized bed. By examining the X-ray images of the fluidized bed, they obtained jet penetration lengths and expansion angles under varied injection conditions. X-ray movies showed the transient jet movement and the interaction between the liquid jet and the fluidized bed. The experiment was carried out in a bed with a cross section of 20 cm by 20 cm and a height of 100 cm. A straight-tube injection nozzle was horizontally inserted into the bed and located about 4 cm above the air distributor plate at the bottom. The nozzle exit (injection point) is 4 cm from the left wall and 10 cm from the front wall. The injection direction is from left to right in the following figures. Experimental conditions are listed in Table 2 together with calculation conditions. Because Ariyapadi et al. focused primarily on liquid jet penetration, the calculated results in this paper focus on jet penetration for different injection and fluidization conditions.

Two sets of injection and fluidization conditions were simulated; these conditions correspond to *Tests L* 1 and *L*3 in Ariyapadi et al. (2003) and parameters are listed in Table 3. The liquid mass flow rate and jet velocity in *Test L* 1 are much smaller than those in *Test L* 3 while the fluidization gas velocity is larger in *Test L* 1. Calculations were run without injection with the gas velocity of *Test L* 3 for 24 s to establish a quasi-steady, fully fluidized bed. Figs. 9d and e show the resulting instantaneous particle volume fraction distribution in the whole fluidized bed and in a thin, center-cut slice, respectively, at 24 s just before liquid injection. The bed is well fluidized but does not exhibit strong bubbling. At 24 s, liquid is injected with conditions of *Test L* 3 and the injection lasted 10 s, which was a typical injection time in the experiment. The *Test L* 1 calculation was started from the previous *Test L* 3 calculation at 24 s with fluidizing gas velocity of 5.6 cm/s. The calculation was run for 6 s for the fluidized bed to reach a quasi-steady condition and at 30 s, and liquid was injected for 10 s.

Fig. 9 compares the liquid injection from the two calculations. Figs. 9a and b show the particles colored by volume fraction mapped to particles for *Test L* 1. With a lower fluidization velocity, *Test L* 3 is less dynamic than *Test L* 1 but it also exhibits good fluidization as seen in Figs. 9d and e. Both the experiment and the Barracuda simulation show similar behavior; however, movies of the experiment showed some liquid agglomeration at the end of the injection time which was not predicted in the simulation. Figs. 9c and f show the liquid distribution 10 s after start of injection. *Test L* 1, with a low liquid feed rate and a high fluidization velocity, has a short penetration length as seen in Fig. 9c. Near the nozzle, particles are primarily liquid (red), and at the end of the jet, which is a few centimeters from the nozzle, liquid particles begin dispersing to other particles through collisions. Fig. 9f shows that the liquid jet at a higher feed rate with the lower fluidizing gas speed penetrates much further into the bed. At the end of the jet, the stream dances about and liquid is transferred to the bed solids through collisions. In both cases, collisions between particles have eliminated liquid particles in upper section of the bed, and there is only a faint gray-red color representing solids with a liquid film.

Ariyapadi et al. (2003) reported the maximum average horizontal distance that the injected liquid penetrates into the bed from the nozzle tip. From movies of the experiment, the jet penetration fluctuates with time in the bubbling bed, and Ariyapadi et al. averaged instantaneous penetration lengths from movie frames to get the injection length. The simulated jet penetration length is calculated the same way by averaging the instantaneous penetration lengths. Fig. 10 shows time snapshots of liquid-particles only (solid and partially wetted solid particles are not shown). The change in liquid-particle size from liquid transfer through collisions is not seen in the figures because particles are shown as pixels and not scaled by their true size. Similar to the experiment, the true penetration length is difficult to measure because older liquid particles are advected by the bed motion back into the injection path. The averaged jet penetration lengths inferred from Fig. 10 for the two test cases are listed in Table 4. Both the experiment and simulation show that the jet penetration in *Test L* 1 is much shorter than that in *Test L* 3. The calculated jet penetration is longer than that reported by Ariyapadi et al. Assuming that Barracuda has calculated bed characteristics well, the calculated longer penetration length suggests that the predicted

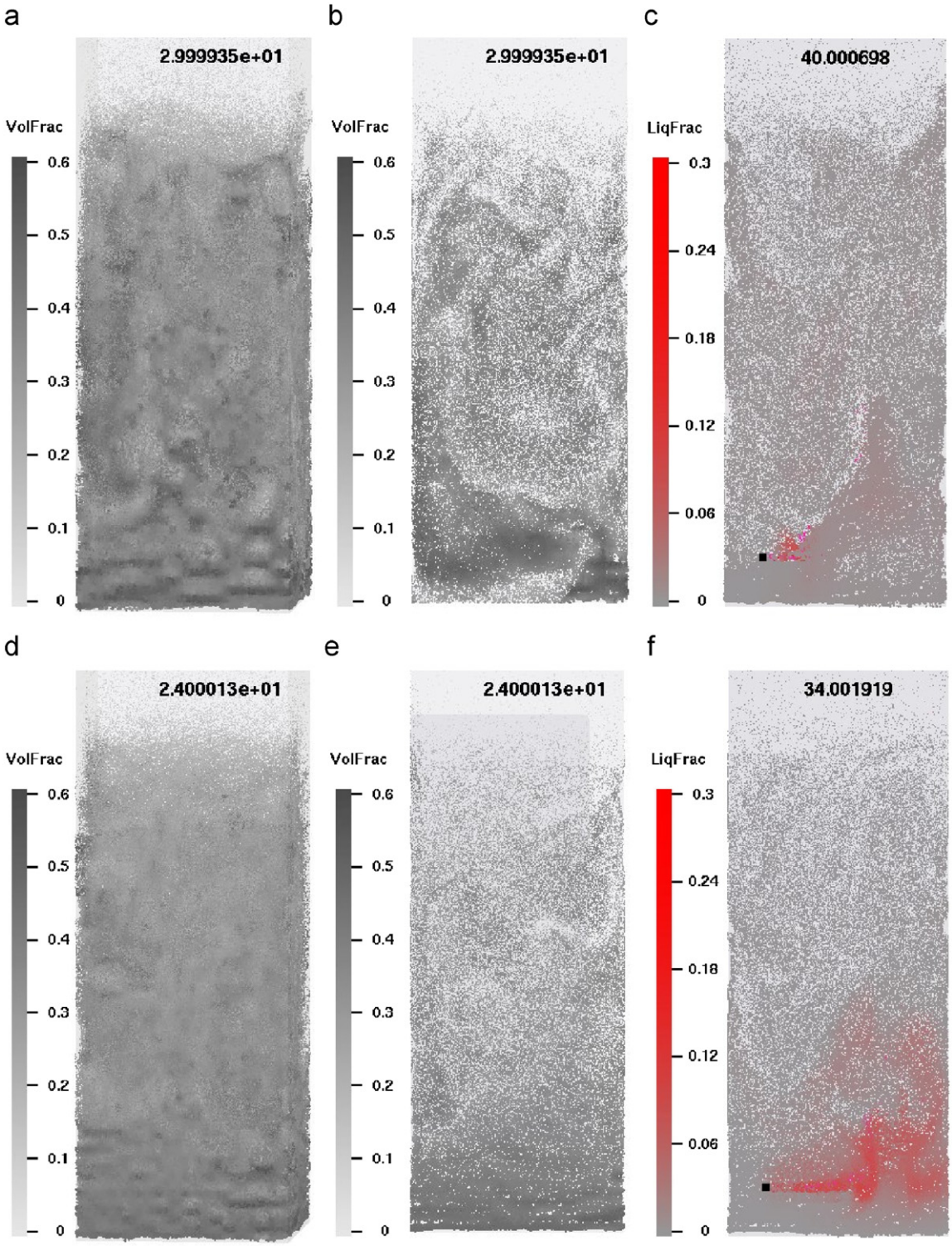

Fig. 9. Snapshots of the fluidized bed before and after liquid injection. Top row: *Test L* 1. Bottom row: *Test L* 3. First column: whole fluidized bed prior to liquid injection with particles colored (gray-scale) by volume fraction. Center column: thin center-slice showing particle colored (gray-scale) by volume fraction prior to liquid injection. Third column: thin center-slice showing particles colored (gray to red) by the fraction of liquid film at 10 s after the injection.

collision frequency is too low. The model requires two relaxation constants K^S and K^L (see Eq. (61)) which could be adjusted to give a better fit to measured penetration data, however, the fidelity of the experiment data is not adequate to provide a better definition of the constants.

8. Summary and conclusions

A new model for the numerical calculation of collisional transfer of mass, momentum, and energy among bed particles in fluidized beds has been developed. The new model is an extension of the

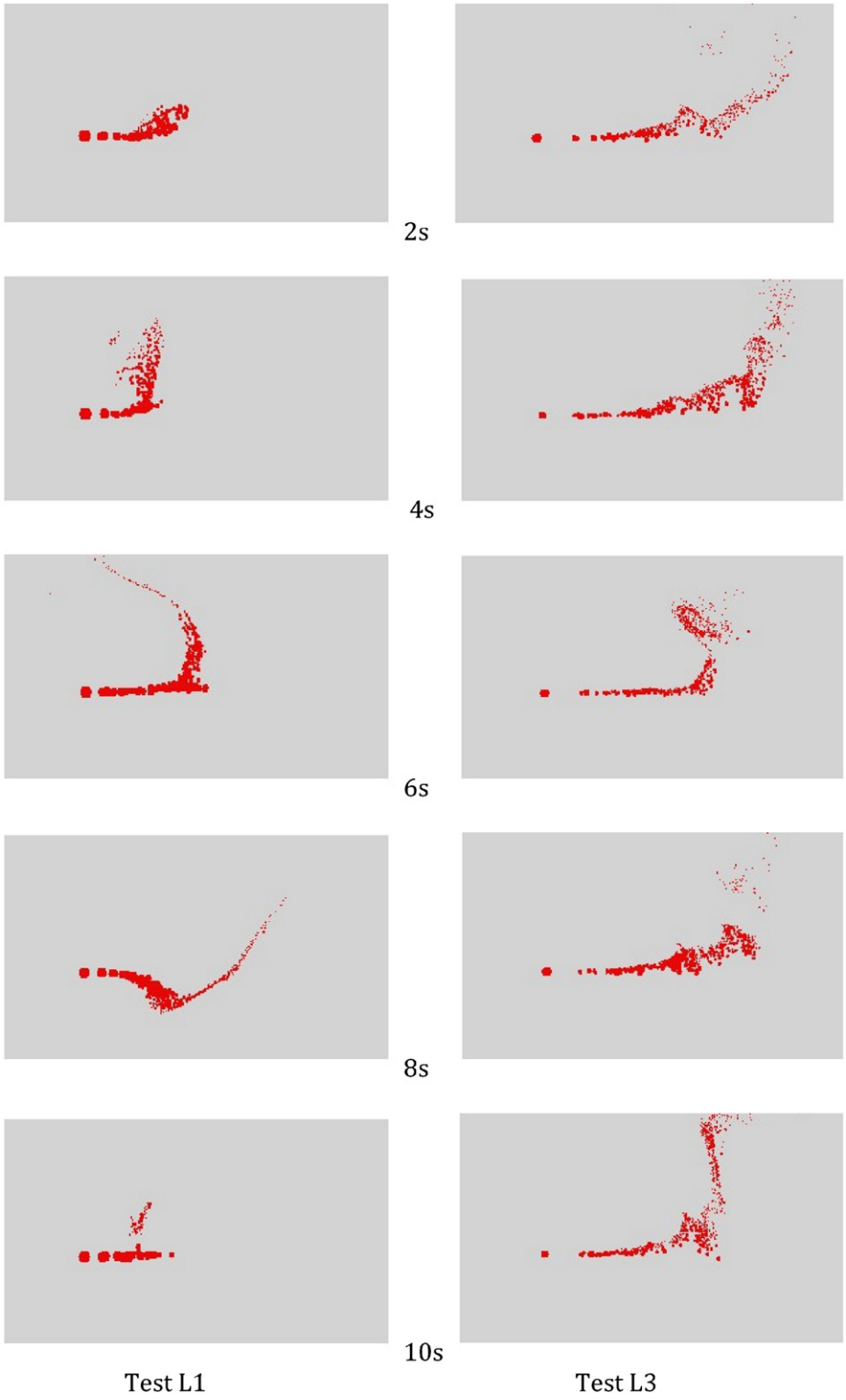

Fig. 10. Calculated liquid droplet distributions at different times after injection, in simulations of the experiments of Ariyapadi et al. (2003). Left column: *Test L* 1. Right column: *Test L* 3. Times after injection are 2, 4, 6, 8, and 10 s from top to bottom.

MP-PIC method for calculating dense particulate flows (Andrews and O'Rourke, 1996; Snider et al., 1998; Snider, 2001) and has been incorporated into the commercial Barracuda code. In this paper we have detailed the equations of the method, the numerical solution procedure for the collision terms, and some properties of the new collision terms. The new collision model resembles the BGK model of gas dynamics (Vincenti and Kruger, 1975), but there are two BGK-like collision terms used to represent the differing rates at which momentum and total equilibrium are achieved.

Table 4
Jet penetration length by experiment and simulation.

Case	Experiment by Ariyapadi et al. (2003)	Current simulation
Test L 1	3.3	5.1
Test L 3	7.3	9.7

The new model has been tested in a series of calculations of liquid injection into a channel of flowing gas and solids, and in calculations simulating the fluidized bed experiments of Ariyapadi et al. (2003). The channel flow calculations demonstrated that the model gives expected trends when injection and channel flow parameters are varied, and that, in this simple channel flow example, momentum equilibrium can be achieved before complete mass transfer between liquid droplets and solid particles has occurred.

In the calculations of the fluidized beds, the simulated appearance of the liquid jets compared well with the movies of the experimental jets, and the expected variations in jet penetration were observed in the calculations when bed and jet velocities were varied. It was not possible to use the experiments to learn about the values of constants in the collision model because of the small number of experiments and the large error bars in the measurements of jet penetration.

Further experiments and simulations are needed to refine the model and determine the values of unknown model constants governing collisional relaxation to equilibrium, and the model needs to be extended to, and tested for, non-isothermal circumstances. These tests and extensions are underway and will be reported in future publications.

Acknowledgments

Partial support for this work was provided by the Department of Energy through the DOE Award DE-FC36-04G014153.

References

Amsden, A.A., et al., 1989. KIVA-II: a computer program for chemically reactive flows with sprays, Los Alamos National Laboratory Report LA-11560-MS.
Andrews, M.J., O'Rourke, P.J., 1996. The multiphase particle-in-cell method (MP-PIC) method for dense particle flow. Int. J. Multiphase Flow 22, 379–402.
Ariyapadi, S., et al., 2003. Digital X-ray imaging technique to study the horizontal injection of gas–liquid jets into fluidized beds, Int. J. Chem. Reactor Eng. 1, Article A56.
Dukowicz, J.K., 1980. A particle-fluid numerical model for liquid sprays. J. Comput. Phys. 35, 229.
Fan, L.S., Zhu, C., 1998. Principles of Gas–Solid Flows. Cambridge University Press, Cambridge.
Gray, M., et al., 2004. Kinetics of cracking and devolatilization during coking of Athabasca residues. Ind. Eng. Chem. Res. 43, 5438–5445.
Heinrich, S., et al., 2003. Study of dynamic multi-dimensional temperature and concentration distributions in liquid-sprayed fluidized beds. Chem. Eng. Sci. 58, 5135–5160.
Lun, C.K., et al., 1984. Kinetic theories for granular flow: inelastic particles in Couette flow and slightly inelastic particles in a general flowfield. J. Fluid. Mech. 140, 223–256.
O'Rourke, P.J., 1981. Collective drop effects on vaporizing liquid sprays. Ph.D Thesis 1532-T, Princeton University.
Savage, S.B., Jeffrey, D.J., 1981. The stress tensor in a granular flow at high shear rates. J. Fluid. Mech. 110, 255–272.
Snider, D.M., et al., 1998. Sediment flow in inclined vessels calculated using multiphase particle-in-cell model for dense particle flows. Int. J. Multiphase Flow 24, 1359–1382.
Snider, D.M., 2001. An incompressible three-dimensional multiphase particle-in-cell model for dense particle flows. J. Comput. Phys. 170, 523–549.
Song, X., et al., 2004. Hydrodynamics of the reactor section of fluid cokers. Powder Technol. 147, 126–136.
Vincenti, W.G., Kruger, C.H. Jr., 1975. Introduction to Physical Gas Dynamics. Robert E. Krieger Publishing Company, Huntington, NY.